

**Polaron absorption for photovoltaic energy conversion in a manganite-titanate *pn* heterojunction**Gesine Saucke,<sup>\*</sup> Jonas Norpoth, and Christian Jooss*Institute for Materials Physics, University of Goettingen, Friedrich-Hund-Platz 1, D-37077 Goettingen, Germany*

Dong Su and Yimei Zhu

*Brookhaven National Laboratory, Upton, New York 11973, USA*

(Received 19 December 2011; published 20 April 2012)

The relation among structure, electric transport, and photovoltaic effect is investigated for a *pn* heterojunction with strong correlation interactions. A perovskite interface is chosen as a model system consisting of the *p*-doped strongly correlated manganite  $\text{Pr}_{0.64}\text{Ca}_{0.36}\text{MnO}_3$  (PCMO) and the *n*-doped titanate  $\text{SrTi}_{1-y}\text{Nb}_y\text{O}_3$  ( $y = 0.002$  and  $0.01$ ). High-resolution electron microscopy and spectroscopy reveal a nearly dislocation-free, epitaxial interface and give insight into the local atomic and electronic structure. The presence of a photovoltaic effect under visible light at room temperature suggests the existence of mobile excited polarons within the band-gap-free PCMO absorber. The temperature-dependent rectifying current-voltage characteristics prove to be mainly determined by the presence of an interfacial energy spike in the conduction band and are affected by the colossal electroresistance effect. From the comparison of photocurrents and spatiotemporal distributions of photogenerated carriers (deduced from optical absorption spectroscopy), we discuss the range of the excited polaron diffusion length.

DOI: [10.1103/PhysRevB.85.165315](https://doi.org/10.1103/PhysRevB.85.165315)

PACS number(s): 75.47.Lx, 73.40.-c, 71.38.-k, 79.20.Uv

**I. INTRODUCTION**

The main constraint for photovoltaic energy conversion in conventional semiconductor *pn* junctions is the limitation to the splitting of the quasi-Fermi energies of photoexcited electrons and holes set by the presence of an energy band gap  $E_g$ . Transmission losses of photons with energies  $E < E_g$  and thermalization losses for  $E > E_g$  determine the Shockley-Queisser limit of photovoltaic energy conversion.<sup>1</sup> It is proposed that the conversion efficiency can be strongly improved by quenching the rapid thermalization process of photoexcited electron-hole pairs and converting such “hot carriers” into a photovoltage.<sup>2,3</sup> Consequently, absorber materials without an optical band gap in the solar spectrum, but with very slow carrier cooling times, are highly desirable.

The *pn* junctions formed by materials with strong electron-electron or electron-phonon interactions offer new opportunities for the study of fundamental mechanisms of solar power generation, e.g., since the band gap and related photovoltaic properties can be tuned by correlation interactions. Especially, correlated materials without gap in the optical absorption spectrum potentially exhibit enhanced lifetimes of photoexcited carriers, e.g., via excitation of small polarons.<sup>4</sup> However, the generally low polaron mobility gives rise to a limited diffusion length of the excited polaron states.

As a model system for the study of photovoltaic effects based on polaronic excitations, we select a heterojunction consisting of *p*-doped  $\text{Pr}_{0.64}\text{Ca}_{0.36}\text{MnO}_3$  (PCMO) and *n*-doped  $\text{SrTi}_{1-y}\text{Nb}_y\text{O}_3$  (STNO;  $y = 0.002$  and  $0.01$ ). The strong electron-phonon interaction in PCMO gives rise to the formation of small polaron states, whose mobility is

dominated by thermally activated hopping.<sup>5-7</sup> The correlation effects in manganites commonly result in a strong tunability of the current-voltage characteristics by temperature, doping, or external fields.<sup>8-11</sup> Previous studies of PCMO-STNO junctions show diode-like current-voltage characteristics<sup>12</sup> and a photovoltaic effect.<sup>13</sup>

Due to their high charge carrier densities, junctions between these heavily doped systems are characterized by space-charge regions on a length scale of a few nanometers, which in turn accentuates the important role of atomistic details of interfacial structure and chemistry. Consequently, in this study we applied high-resolution electron microscopy and spectroscopy in combination with electrical transport measurements and optical absorption spectroscopy to yield a comprehensive picture of the interfacial structure, band scheme, and photovoltaic properties.

**II. EXPERIMENTAL PROCEDURE**

Epitaxial perovskite *pn* heterojunctions were fabricated by reactive ion-beam sputtering from a stoichiometric target at deposition temperature  $T_{\text{dep}} = 750^\circ\text{C}$  and oxygen partial pressure  $p_{\text{O}_2} = 10^{-4}$  mbar. PCMO thin films with thicknesses of 200 and 380 nm were deposited into a  $5 \times 5$  mm<sup>2</sup> shadow mask on polished STNO(100) substrates with  $y = 0.002$  or  $y = 0.01$  Nb doping. Ohmic contacts on STNO are obtained by sputtered Ti contacts with a thin Au protection coating, while nearly ohmic behavior is found for Au contacts ( $\sim 150$  nm) on PCMO. All metal contacts were deposited into  $1.5 \times 4.5$  mm<sup>2</sup> shadow masks at  $T_{\text{dep}} = 200^\circ\text{C}$ . A schematic representation of the setup is provided in Fig. 5(a).

For optical absorption spectroscopy a 140-nm PCMO film was deposited on a polished  $(\text{LaAlO}_3)_{0.3} - (\text{Sr}_2\text{AlTaO}_6)_{0.7}$ (100) substrate by pulsed laser deposition from a stoichiometric target at  $T_{\text{dep}} = 750^\circ\text{C}$ ,  $p_{\text{O}_2} = 0.2$  mbar, and a laser fluence  $F = 1.5$  J/cm<sup>2</sup>.

Published by the American Physical Society under the terms of the [Creative Commons Attribution 3.0 License](https://creativecommons.org/licenses/by/3.0/). Further distribution of this work must maintain attribution to the author(s) and the published article's title, journal citation, and DOI.

Structure analysis includes x-ray diffraction (XRD), (scanning) transmission electron microscopy [(S)TEM] and electron energy-loss spectroscopy (EELS). STEM and EELS analysis was performed with Brookhaven's Hitachi HD-2700 STEM with a  $C_s$ -corrected probe.<sup>14</sup> Cross-section samples for TEM analysis were prepared with a focused ion beam and subsequent low-energy Ar ion milling. A Varian Cary 5e was used for optical absorption spectroscopy with unpolarized light.

Electrical measurements were conducted in two-point geometry with supply-line resistances excluded [see inset in Fig. 5(a)] in a cryostat with a Suprasil window. Illumination of the samples for photovoltaic measurements was provided by a mercury pressure lamp, whose power spectrum extends from 0.5 to 5 eV, with a roughly constant regime below 2 eV and strong lines at higher energies.

### III. RESULTS AND DISCUSSION

#### A. Interface structure and band scheme

XRD reveals [001] growth of the PCMO films ( $Pbnm$  notation) with an epitaxial in-plane relation PCMO[100]  $\parallel$  STNO[110] ( $Pm\bar{3}m$  notation). Cross-section TEM confirms the coherent epitaxy of the PCMO-STNO interface and reveals a low density of misfit-dislocation (roughly three dislocations per 10  $\mu\text{m}$ ). A minor portion of misoriented grains appears near the surface of the PCMO films, which are also detected as surface islands with atomic force microscopy.

Figure 1(a) shows a high-resolution STEM image of the PCMO-STNO junction in high-angle annular dark-field (HAADF) mode. In the perovskite structure, cations with high ionic radii (Sr or Pr/Ca) occupy the so-called A site, while smaller ions (Ti/Nb or Mn) reside on the B site. Since HAADF imaging is sensitive to atomic mass number ( $Z$  contrast), Fig. 1(a) suggests a stacking order of Sr-Ti(Nb)-Pr(Ca)-Mn as depicted in the scheme. The chemical composition derived from EELS line scans in Fig. 1(b) reveals a subtle offset of the

inflection points of the A- and B-site profiles, by approximately 0.5 nm, and a distinct interdiffusion of Ti into the PCMO. The individual concentration profiles are fitted with error functions to extract the roughness parameter  $\sigma$  ( $2\sigma$  indicates the width corresponding to a concentration decrease from 84% to 16%). For the sample with 200-nm PCMO film, we find  $\sigma_{\text{Pr+Ca}} = 0.68(2)$  nm,  $\sigma_{\text{Sr}} = 0.56(5)$  nm,  $\sigma_{\text{Ti,STNO}} = 0.82(12)$  nm,  $\sigma_{\text{Mn,STNO}} = 0.96(21)$  nm,  $\sigma_{\text{Ti,PCMO}} = 1.60(32)$  nm, and  $\sigma_{\text{Mn,PCMO}} = 1.78(44)$  nm, each averaged over several line scans at different positions. The asymmetric B-site profiles are fitted in STNO and PCMO separately. Similar numbers are found for the 380-nm PCMO sample. Note that a systematic overestimate of the determined roughness must be taken into account due to the finite size of the probe diameter (0.2 nm) and the finite thickness of the specimen lamella.

The increased width and the asymmetric shape of the B-site profiles affect the electronic structure of the interface: in PCMO the substitution of Mn with a formal valence of  $3.36+$  by  $\text{Ti}^{4+}$  reduces the  $p$ -doping level. A nominal transition from  $p$  to  $n$  doping takes place, where the absolute concentration of Ti is larger than that of Ca. Based on this criterion, a shift of the electronic  $pn$  interface toward the PCMO side by slightly less than 1 nm can be estimated from Fig. 1(b).

The B-cation interdiffusion and the associated change in the doping level also influence the position and width of the space-charge layer around the junction. The formal electron (hole) doping level in STNO (PCMO) is given by the density of the doping Nb (Ca) cations and amounts to  $n = (0.3\text{--}1.7) \times 10^{20} \text{ cm}^{-3}$  for  $y = 0.002\text{--}0.01$  and  $p = 6.4 \times 10^{21} \text{ cm}^{-3}$ . As Hall-effect measurements in the related small-polaron regime of  $\text{La}_{0.7}\text{Ca}_{0.3}\text{MnO}_3$  reveal an effective hole carrier density, which amounts to roughly 60% of the formal density,<sup>15,16</sup> this is also considered for PCMO in the following. Based on the solution of the Poisson equation for a sharp heterojunction,<sup>17</sup> space-charge layers of  $x_n = 10\text{--}51$  nm hold for the STNO side of the junction, but only  $x_p = 0.2\text{--}0.7$  nm on the PCMO side (dependent on Nb doping and temperature; dielectric constants  $\epsilon^{\text{STO}} = 306/1500$  and  $\epsilon^{\text{PCMO}} = 30/30$  at  $T = 300/80$  K taken

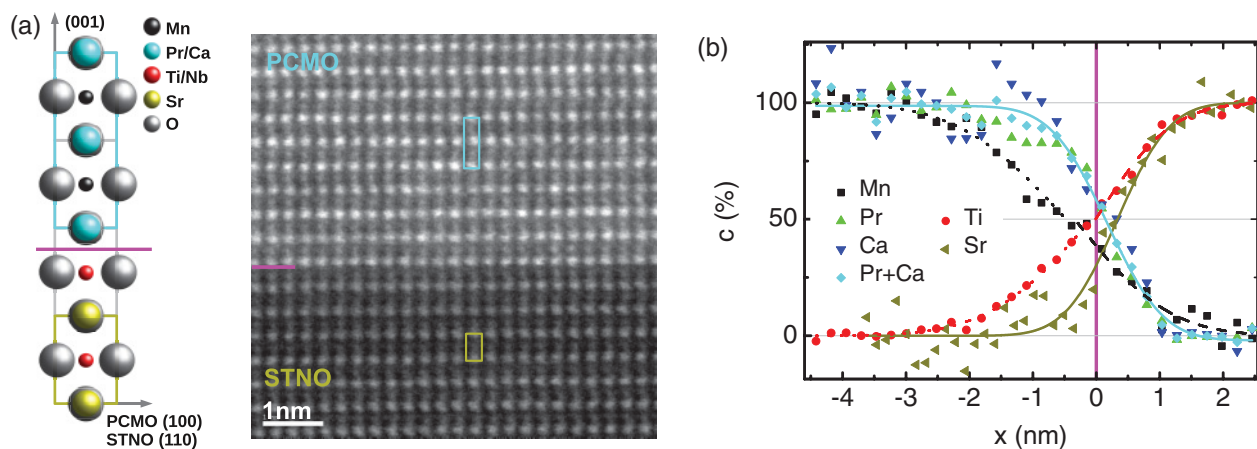


FIG. 1. (Color) Structure and chemical composition of the PCMO-STNO junction (film thickness  $d = 200$  nm,  $y = 0.01$ ,  $T \approx 80$  K). (a) HAADF-STEM image of a cross section of the interface along the [110]-STNO zone axis (collection angle: 114–608 mrad). The projected structure and stacking order are schematically depicted on the left and the subunit cells are marked on the STEM image. (b) Profile of the chemical composition across the interface deduced from simultaneous acquisition of appropriate core-loss spectra in EELS line scans. Measured signal integrals (symbols) are fitted with error functions (lines). The interface is shown as a pink line in all images.

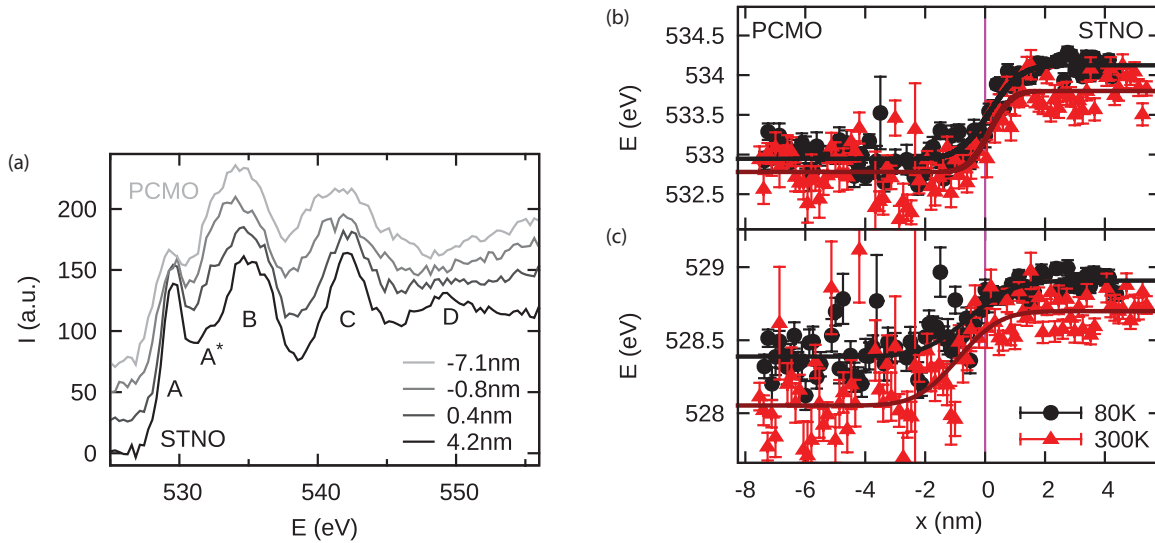


FIG. 2. (Color online) Evolution of the O K ELNES across the PCMO-STNO junction (film thickness  $d = 380$  nm,  $y = 0.002$ ). (a) Individual point spectra ( $5\times$  binned) acquired at different distances from the interface at room temperature. Reference to the features labeled A–D is given in the text. (b, c) Detailed evolution of the peak centers of the ELNES features A and B across the interface at room temperature and  $T \approx 80$  K. Gaussian fits to individual spectra (symbols) are fitted with error functions (lines). The interface position ( $x = 0$ ) is defined as specified in Fig. 1.

from Refs. 18–20). As B-cation interdiffusion takes place on a sub-2.5-nm scale on both sides of the junction, it mainly affects the space-charge region of the PCMO and, presumably, leads to a pronounced enlargement compared to its nominal width.

Further insight into the electronic structure of the junction is provided by the energy-loss near-edge structure (ELNES) of core-loss edges, since it probes transitions to the first unoccupied states above the Fermi level. Figure 2(a) shows the ELNES of the O K edge (O  $1s \rightarrow$  O  $2p$  transition) at different distances to the junction. Comparison with band structure calculations for SrTiO<sub>3</sub> (STO)<sup>21</sup> and Pr<sub>0.5</sub>Ca<sub>0.5</sub>MnO<sub>3</sub><sup>22</sup> yields a precise assignment of the individual ELNES features. For STO, the features in Fig. 2(a) labeled A, A\*, B, C, and D are related to hybridization of O  $2p$  orbitals with Ti  $3d t_{2g}$ , Ti  $3d e_g$ , Sr  $4d$ , Sr  $5p$ , and Ti  $4sp$  states. In PCMO, feature A corresponds to hybridization with Mn  $3d e_g \uparrow$  (spin up), and the broad feature B to hybridization with Mn  $3d t_{2g} \downarrow$ , Mn  $3d e_g \downarrow$ , and Pr and Ca states. The spectra most distant from the interface in Fig. 2(a) show bulk-like characteristics.

The slight interdiffusion of Ti and the resulting shift of the electronic  $pn$  interface toward the PCMO side is reflected in the evolution of the O K A-peak energy across the junction [Fig. 2(b)], since it is exclusively related to O  $2p$ –Mn  $3d$  and  $-\text{Ti } 3d$  hybridization. The corresponding evolution of the O K B-peak energy [Fig. 2(c)], which is dominated by hybridization with A-site cations, reveals a sharper transition and its inflection point is shifted compared to the Ti/Mn interface position (compare Fig. 1).

Since the onset of the O K edge reflects transitions to the first empty states above the Fermi level, the evolution of the O K A-peak energy approximately traces the local electron affinity  $\chi$ . This is particularly valid, since the O  $1s$  orbital is not involved in hybridization and thus represents a constant reference level across the junction. Therefore, the offset between the bottom edges of the conduction bands in STNO and PCMO can be read

off directly from Fig. 2(b) as  $\Delta\chi = 0.65(4)/0.57(5)$  eV at  $T = 300/80$  K. As its transition width is much narrower than  $x_n$  and a substantial part of the built-in voltage  $V_D = 0.76$  V (the work function difference)<sup>23,24</sup> drops in the STNO side of the junction ( $V_{D,p}/V_{D,n} = n\epsilon_n/p\epsilon_p$ ), the measured  $\Delta\chi$  indicates the presence of an energy spike in the conduction band and a reverse barrier  $\phi_B = \Delta E_C - V_{D,p}$  for electrons from the PCMO side. Here, the ideal conduction band discontinuity  $\Delta E_C = \Delta\chi$  can be reduced due to the interdiffusion of Ti and Mn.

Upon cooling with liquid nitrogen to  $T \approx 80$  K, electron diffraction reveals the emergence of a twofold superstructure along the crystallographic  $b$  direction (not shown) as evidence for the charge-ordered  $P2_1mn$  phase in PCMO.<sup>25</sup> The corresponding shift of the O K A-peak energy to higher values [see Fig. 2(b)] is consistent with the opening of a charge gap as reported from optical spectroscopy.<sup>26</sup> The analogous shift in the STNO reflects its well-known low-temperature band-gap widening.<sup>27</sup> Our own measurements of the optical absorption coefficient of PCMO in Fig. 3 support the picture of a gap opening upon cooling below the charge-ordering temperature  $T_{CO} \approx 230$  K. The spectra exhibit a broad absorption band centered around 1.5 eV, which can be attributed to small polaron absorption.<sup>28,29</sup>

Figure 4 gives a schematic summary of the aforementioned considerations in the form of a single-particle band scheme across the PCMO-STNO junction. We stress this single-particle representation only to illustrate the relative equilibrium positions of the respective states around the Fermi level and the characteristics of the energy spike in the conduction band of the STNO. Correlation effects governing localization and polaron formation in PCMO cannot be taken into account in this simplified picture, especially not in terms of excited states. Since both materials exhibit high doping levels, the PCMO valence band edge is assumed to be nearly

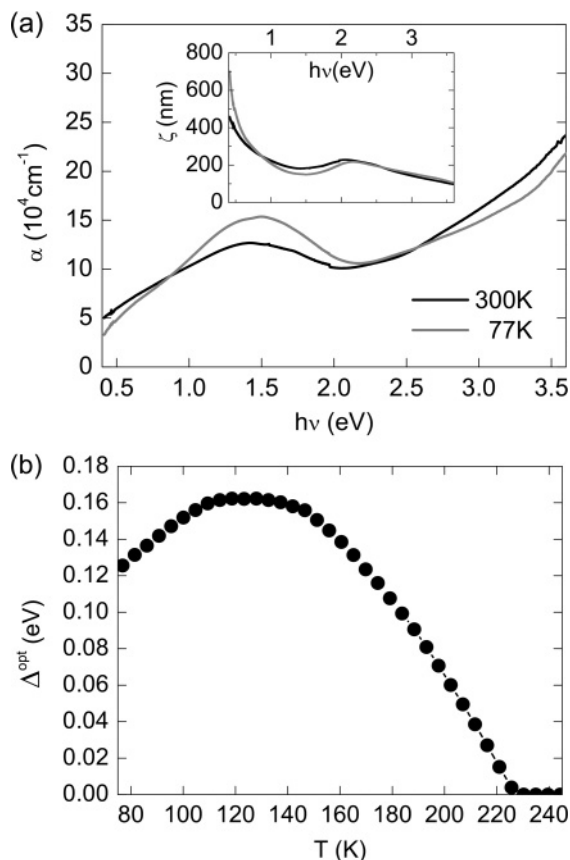


FIG. 3. Optical properties of PCMO thin film. (a) Absorption coefficient  $\alpha$  in the NIR-VIS spectral range at selected temperatures. Inset: Corresponding penetration depth  $\zeta$  indicating the decrease in the incident illumination intensity by 90%. (b) Temperature dependence of the optical gap  $\Delta^{\text{opt}}$  extracted from the abscissa intercept of linear fits to the low-energy tail of the absorption coefficient spectra.

aligned to the STNO conduction band edge. Based on the low defect density at the interface, Fermi level pinning effects due to interface states are not considered. The ideal and the interdiffusion-smoothed energy spike in the conduction band are both schematically depicted. Since the interdiffusion of Mn into STNO only takes place on a small length compared to the width of the space-charge layer, an accompanying decrease in the STNO band gap at the interface should not entirely suppress the energy spike. This is also supported by the determination of the activation energy for electrical transport across the junction presented in the next section.

### B. Transport properties I: Equivalent circuit analysis

The current-voltage curves of the PCMO-STNO junction in Fig. 5(a) exhibit rectifying characteristics at all temperatures. In order to gain insight into the detailed mechanisms governing the electric transport across the junction, we interpret the current-voltage characteristics in terms of an equivalent circuit consisting of a diode, a series resistance  $R_S$ , and a parallel resistance  $R_p$ . The corresponding current density-voltage

relation is given by

$$J(U) = J_S \left[ \exp\left(\frac{e(U - Jr_S)}{nk_B T}\right) - 1 \right] + \frac{U - Jr_S}{r_p}, \quad (1)$$

where  $e$  is the elemental charge,  $k_B T$  is the thermal energy, and  $r_S = R_S A$  and  $r_p = r_p A$  are the resistances times contact area  $A$ . The deviation from ideal diode behavior is described by the ideality factor  $n$ . The corresponding temperature dependence of the saturation current density can be written as

$$J_S = J_{00} \exp\left(\frac{-E_A}{nk_B T}\right), \quad (2)$$

where  $J_{00}$  only slightly depends on temperature. The activation energy  $E_A$  and  $n$  both depend on the electronic structure of the  $pn$  junction and the associated mechanism of electron transfer.<sup>33–35</sup>

From Eq. (1),  $J_S$  and  $n$  can be determined by a linear fit to  $\ln(J)$  in that voltage regime, where the current is dominated by the diode and the influence of  $R_S$  and  $R_p$  can be neglected, i.e., the regime with the highest local slope in the forward branch.  $J_S$  is then given by the ordinate intercept and  $n$  is calculated from the slope. The series resistance can be estimated as  $R_S = \Delta U / I^{\text{max}}$  from the voltage difference  $\Delta U$  between the extrapolated linear fit and the measured curve in the high-current regime, which is dominated by  $R_S$  [here  $I^{\text{max}} = 10 \text{ mA}$ ; see Fig. 5(a)].

The results of this analysis are presented in Figs. 5(b)–5(d). At first, we concentrate on the two samples with 380-nm-thick PCMO films. (Note that below  $T = 50 \text{ K}$  the analysis is heavily flawed by the undifferentiated characteristics at low voltages, the high  $R_S$  and hysteretic effects.) The temperature dependence of  $R_S$ , which is the sum of contributions from PCMO film, STNO substrate, and contact resistances, is mainly governed by the thermally activated conductivity of the PCMO. Remembering that the resistance of PCMO is a nonlinear function of the applied voltage, the trend in Fig. 5(b) thus underestimates its temperature-dependent increase. The resistance of the substrate yields a significant contribution only at elevated temperatures, as is obvious from the doping trend. The ideality factor shows an increase upon cooling from  $n \simeq 1.4$  to  $n > 2$ . An increase above  $n = 1$ , the value for an ideal diode, occurs, e.g., by Shockley-Read-Hall recombination via traps in the space-charge region ( $1 < n \leq 2$ ) or by tunneling-enhanced recombination at the interface or in the space-charge region ( $n > 2$ ).<sup>33</sup> The strong increase in  $n$  in the PCMO-STNO junctions at low temperatures points toward important contributions of tunneling processes.  $J_S$  exhibits an exponential decrease with temperature as expected from Eq. (2). Its strong increase with the Nb-doping level is incompatible with a diffusion-controlled transport process. Instead, the energy spike appears to be the relevant barrier since its width and the height of the reverse barrier decrease with higher  $n$  doping.

Strong evidence for the dominant role of the energy spike originates from the magnitude of the activation energy as discussed in the following. According to Eq. (2), it can be determined as the slope of a plot  $n \cdot \ln(J_S)$  vs inverse temperature and amounts to  $E_A = 761(7) \text{ meV}$  ( $y = 0.002$ ) and  $E_A = 603(2) \text{ meV}$  ( $y = 0.01$ ), respectively (determined in the cooling branch). For a  $pn$  heterojunction with continuous

band bending and only small reverse barriers, the electron transfer can take place via a diffusion current as in a homojunction. Shockley's diffusion model yields  $n = 1$  and the activation energy is given by the band gap  $E_A = E_g$ . In the case of a heterojunction, the smaller band gap determines the transport,<sup>33,34</sup> thus here  $E_A = E_{g,p}$  with  $E_{g,p} \leq 0.18$  eV (see Fig. 4). For Shockley-Read-Hall recombination, the activation energy is lower or equals the size of the smaller band gap  $E_A \leq E_{g,p}$ , depending on the depth of the involved trap levels.<sup>36</sup> If an energy spike in the conduction band is present, the mechanism of electron transfer can change from diffusion to thermionic emission. The spike gives rise to a reverse barrier  $\phi_B$  and leads to an increased activation barrier  $E_A = E_{g,p} + \phi_B$ .<sup>34</sup> Since  $\phi_B \approx \Delta\chi$ , the determined activation energies  $E_A$  roughly match the values determined by EELS in the previous section [ $\Delta\chi = 0.65(4)/0.57(5)$  eV at  $T = 300/80$  K for  $y = 0.002$ ]. The doping trend supports the identification of  $E_A$  with the energy spike in the conduction band of the STNO, since the Nb level cannot affect the magnitude of the PCMO band gap. Instead, an increase in the  $n$ -doping level enhances the built-in voltage drop on the  $p$  side of the junction and therefore reduces  $\phi_B$ .

In the following, we discuss the deviating trends in the junction parameters of the sample with the 200-nm PCMO film [see again Figs. 5(b)–5(d)]. On the cooling branch, the sample initially behaves like its thicker counterpart, but below  $T = 125$  K it deviates distinctively. The subsequent heating branch constitutes a hysteresis closing at  $T = 250$  K. We interpret this observation as emergence of the colossal

electroresistance (CER) effect in the PCMO, i.e., the melting of the low-temperature, charge- and orbital-ordered phase by the combined action of electrical current and electric field.<sup>6,7,37–39</sup> The sharp drop in the resistance of the PCMO, as reflected by  $R_S$ , is a characteristic feature of the accompanying insulator-metal transition. A direct comparison with the critical quantities necessary to induce the CER given in Refs. 6 and 7 is restricted by the differences in the particular measurement geometries, namely, *cross-plane* vs *in-plane*. Nonetheless, it is established therein that the CER is not a unique function of temperature, electrical current and electric field but, rather, depends on their complex interplay and the sample history. In our concrete top-bottom measurement geometry, we argue, that the high electric field (50 kV/cm at 1-V voltage drop across the PCMO) is the basic driving force for the phase transition. The CER increases the ideality factor and reduces the activation energy, namely, from  $E_A = 747(9)$  meV to  $E_A^{\text{CER}} \approx 559$  meV. We interpret this as a decrease in the effective barrier height due to enhanced tunneling contributions, i.e., thermionic field emission: the collapse of the PCMO band gap in the CER regime provides additional, low-lying final states for electrons tunneling through the energy spike from STNO to PCMO. The decrease in the effective barrier height is also reflected in a pronounced increase in the saturation current density.

The slight hysteretic features in the respective parameters of the 380-nm PCMO sample with  $y = 0.002$  suggest that also therein a minor volume portion might be affected by the CER at low temperatures.

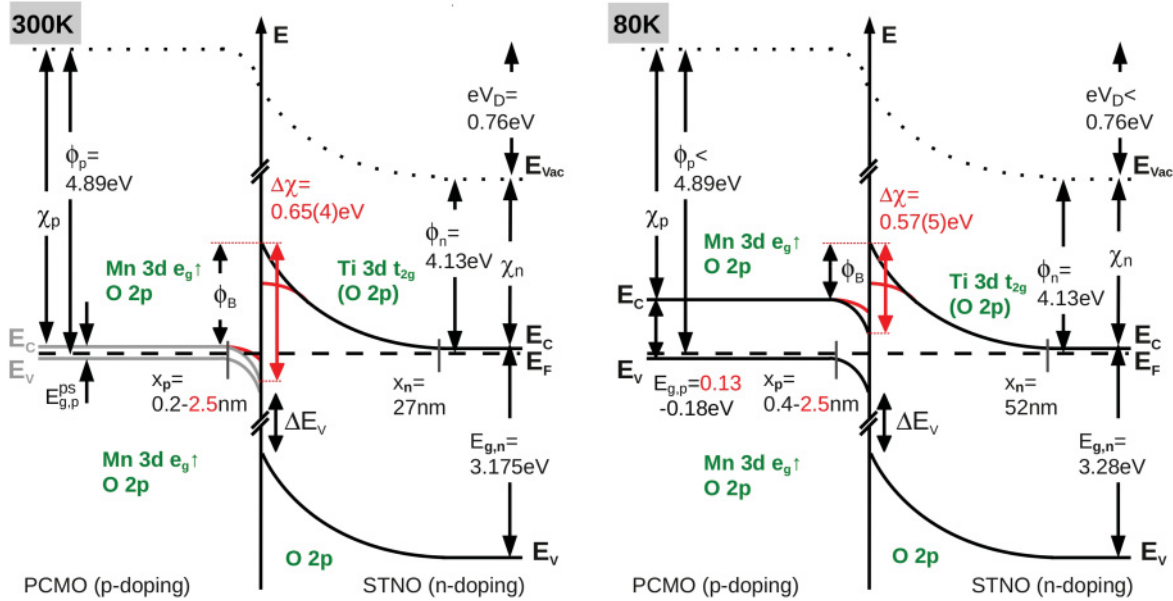


FIG. 4. (Color) Band scheme of the PCMO-STNO ( $y = 0.002$ ) junction at room temperature and  $T \approx 80$  K. Data based on our measurements are depicted in red. The predominant orbital character of states contributing to conduction and valence bands ( $E_C$  and  $E_V$ ) as derived from the calculated density of states for PCMO<sup>22</sup> and STNO<sup>30</sup> is noted in green. Above the charge-ordering temperature ( $T_{\text{CO}} \approx 230$  K), PCMO exhibits a polaronic pseudogap  $E_{g,p}^{\text{ps}}$ , e.g., a pronounced depression of the density of states at the Fermi level  $E_F$  separating occupied and empty states of predominant Mn  $e_g$  character.<sup>31</sup> The diffusion potential  $V_D = \Phi_p - \Phi_n$  equals the difference in the work functions,<sup>23,24</sup> while the conduction band discontinuity  $\Delta E_C$  is given by the difference in the electron affinities  $\Delta\chi$  in the case of an abrupt interface. Due to the discontinuity, there is a reverse barrier  $\phi_B$  for electrons from the PCMO side. Below  $T_{\text{CO}}$ , the PCMO Fermi level shifts to higher values,<sup>32</sup> slightly decreasing  $V_D$ . The values for the band gap  $E_{g,n}$  in STO are taken from Ref. 27; in PCMO  $E_{g,p}$  opens below  $T_{\text{CO}}$ .<sup>26</sup> For both temperatures, the existence of an energy spike in the conduction band is evident, but its height as well as the width of the space charge regions (mainly  $x_p$ ) is affected by the Ti/Mn interdiffusion (see text).

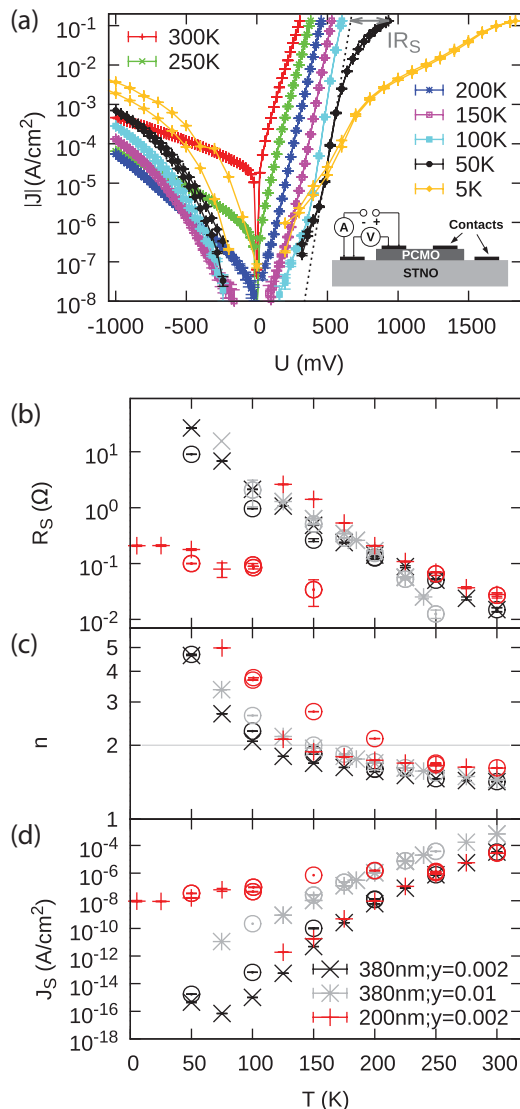


FIG. 5. (Color online) Temperature-dependent current-voltage characteristics of the PCMO-STNO junctions without illumination. (a) Selected  $J$ - $U$  curves of the 380-nm PCMO sample with  $y = 0.002$ . Inset: Sample and measurement setup as described under Experimental Procedure. The arrow exemplifies the determination of  $R_S$ ; see text for details. For all samples, the appropriate parameters of the equivalent circuit model analysis (see text) are given in (b) series resistance  $R_S$ , (c) ideality factor  $n$ , and (d) saturation current density  $J_S$ . Crosses (circles) represent the cooling (heating) branch.

### C. Transport properties II: Photovoltaic effect and photocarrier diffusion length

Illumination of the PCMO films generates a photovoltaic effect in the complete temperature interval under consideration as presented in Fig. 6. The observation of a photovoltaic effect is most remarkable above the charge-ordering transition temperature, where a band gap in the PCMO absorber is absent. The strong impact of a 2.3-eV high-pass filter on the photovoltaic properties, demonstrated in Fig. 6(a), is discussed later.

The photovoltaic short-circuit current  $I_{SC}$  in Fig. 6(b) is most pronounced in the sample with the thinnest PCMO absorber, whose thickness is admittedly already comparable with the mean photon penetration depth [see Fig. 3(a)]. We

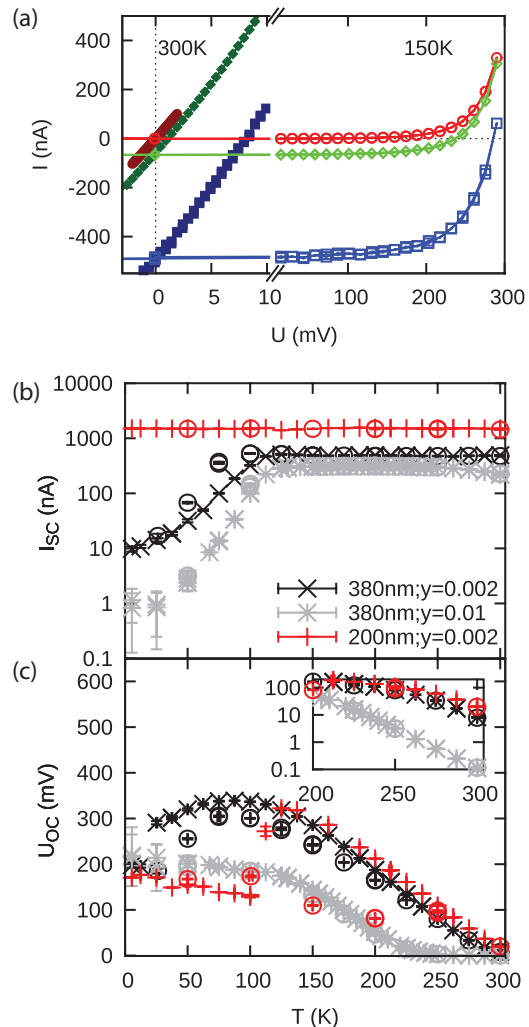


FIG. 6. (Color online) Temperature-dependent photovoltaic effect of the PCMO-STNO junction. (a) Current-voltage characteristics in the dark [(red) circles] and under illumination with a Hg lamp [(blue) squares] or an additional 2.3-eV high-pass filter [(green) diamonds] of the 380-nm PCMO sample with  $y = 0.002$ . Dark-colored filled symbols represent measurements at room temperature; light-colored open symbols mark measurements at  $T = 150$  K below the charge-order transition. Solar cell parameters under unfiltered Hg lamp illumination, i.e., (b) short-circuit photocurrent  $I_{SC}$  and (c) open-circuit voltage  $U_{OC}$ , are represented by crosses (circles) for the cooling (heating) branch. The inset in (c) is a zoom of the high-temperature regime.

assume that the difference between the samples with 380-nm PCMO is due to slight deviations from their nominal thickness. We interpret the decrease in  $I_{SC}$  in the thick samples at low temperatures as an effect of the vanishing carrier mobility in the PCMO, which, in contrast, is maintained in the thin sample due to the CER.

Neglecting the influence of parallel resistance, the open-circuit voltage reads, from Eq. (1),

$$U_{OC}(T) = \frac{nk_B T}{e} \ln \left( \frac{J_{SC}}{J_S} + 1 \right) \quad (3)$$

$$\approx \frac{E_A}{e} - \frac{nk_B T}{e} \ln \left( \frac{J_{00}}{J_{SC}} \right), \quad (4)$$

where  $\ln(J_{00}/J_{SC}) > 0 \forall T$  and the approximation holds for  $J_{SC} \gg J_S$ , i.e., below  $T \approx 200\text{--}250$  K, depending on the sample. Consistent with this relation, Fig. 6(c) exhibits a roughly linear increase in  $U_{OC}$  at the early cooling stages and saturation at lower temperatures, where  $n$  and  $I_{SC}$  begin to increase and decrease, respectively. The offset between the curves for samples with different Nb-doping levels amounts to  $\Delta U_{OC} \approx 150$  mV. In accordance with Eq. (4), this value nicely coincides with the difference in the respective activation energies determined in the previous section. (A precise estimate of  $E_A$  by linear fits to  $U_{OC}$  is hindered by the temperature dependence of  $n$ .)<sup>35</sup> Correspondingly, the decrease in the activation energy due to the CER in the 200-nm PCMO sample,  $\Delta E_A^{CER} \approx 190$  meV (see the previous section) is reflected by an analogous drop in  $U_{OC}$ . Furthermore, the related photovoltage drop in the 380-nm PCMO sample with  $y = 0.002$  again indicates a CER impact at very low temperatures.

Concerning the source of the observed photocurrents, three contributions have to be taken into account: (i) excitations above the STNO band gap in the substrate, (ii) excitations directly above the spike within the space-charge region of the PCMO (pSCR), and (iii) polaronic excitations in the PCMO absorber. In order to discriminate among the different contributions, a 2.3-eV high-pass filter was inserted in front of the Hg lamp to exclude the PCMO polaron absorption peak [see Fig. 3(a)]. In the temperature range 150–300 K, this leads to a drop in  $I_{SC}$  by 83% (sample with 200-nm PCMO film and  $y = 0.002$ ), 88% (380 nm,  $y = 0.002$ ) and 85% (380 nm,  $y = 0.01$ ), respectively (not shown as a separate figure). Therefore, at elevated temperatures, only a minor part of the photocurrent in these samples stems from excitations within the wide-gap STNO substrates; instead, low-energy excitations in the PCMO side of the junction dominate. At lower temperatures, the influence of the CER again draws a distinction between samples with thin and those with thick PCMO layers: the portion of the low-energy excitations in  $I_{SC}$  remains at 83% down to  $T = 5$  K in the case of the CER-affected 200-nm PCMO absorber, while in the 380-nm PCMO samples almost the whole photocurrent is generated from excitations by photons with  $E > 2.3$  eV below  $T = 80$  K. We return to this important observation later.

The nature of the photoexcited minority carriers in the PCMO, especially their mobility and lifetime, is a central issue concerning its potential as an efficient photovoltaic absorber material. In this context, a question arising from our measurements is whether the observed photocurrent at elevated temperatures stems from photocarriers in the PCMO (iii) or whether it is dominated by excitations in the pSCR (ii), i.e., rather like excitations of electrons from a metal directly above the spike, as in an n-type Schottky solar cell. To further elucidate these individual contributions, we concentrate in the following on that part of the photocurrent which is generated by low-energy excitations  $I_{SC}^{low}$ , i.e., the difference between  $I_{SC}$  obtained by illumination with the full Hg spectrum and that obtained with the additional 2.3-eV high-pass filter respectively. From the measurement of the optical absorption coefficient [compare Fig. 3(a)], we can deduce a penetration-depth-dependent electron-hole pair generation rate  $g(z, \lambda) = \alpha(\lambda) \cdot P(z, \lambda)/E(\lambda)$  and compare it with the actual number of

electrons carrying  $I_{SC}^{low}$ ,  $n_{SC}^{low} = I_{SC}^{low}/(A \cdot e)$ . Here,  $z$  denotes the penetration depth into the PCMO absorber,  $\lambda$  the photon wavelength,  $E$  the photon energy,  $\alpha$  the absorption coefficient,  $P$  the local illumination power density per wavelength (in  $\text{mW cm}^{-2} \text{ nm}^{-1}$ ) deduced from the Lambert-Beer law with the given  $\alpha$ ,  $A = 0.5 \times 0.2 \text{ cm}^2$  the illuminated area of the PCMO absorber, and  $e$  the elemental charge. Taking into account 5% absorption loss due to the cryostat entrance window and 10% reflection loss at the sample surface as deduced from ellipsometry, an incident illumination power  $P(0, \lambda) = 6 \times 10^{-3} \text{ mW cm}^{-2} \text{ nm}^{-1}$  for the photovoltaic measurements is used for the calculation of  $g(z, \lambda)$ . (Note that the quantum efficiency is set to unity, i.e., every absorbed photon generates one electron-hole pair.) Thus, given both the spatiotemporal distribution of photoexcited minority carriers in the sample and the resulting photocurrent, we now try to determine the effective "inflow region" of photocarriers to the heterojunction.

The mean free path before recombination for photoelectrons in PCMO is given by the diffusion length  $L$ , which thus represents the radius of a "habitat sphere" around the locus of the initial photocarrier generation. As depicted in the inset in Fig. 7, the interpenetrating volume of this sphere with the pSCR and STNO is considered as a measure of the probability that the appropriate photoelectron will reach the accelerating built-in field of the SCR and potentially contribute to  $I_{SC}^{low}$ . Given the high intrinsic carrier density in PCMO, we propose that Auger recombination is the dominant recombination mechanism. In the previous section, we demonstrated that the interfacial energy spike in the conduction band dominates the transport properties of the junction. Since this energy barrier constricts photoelectrons to enter STNO, the recombination is effectively increased by the junction and we assign a

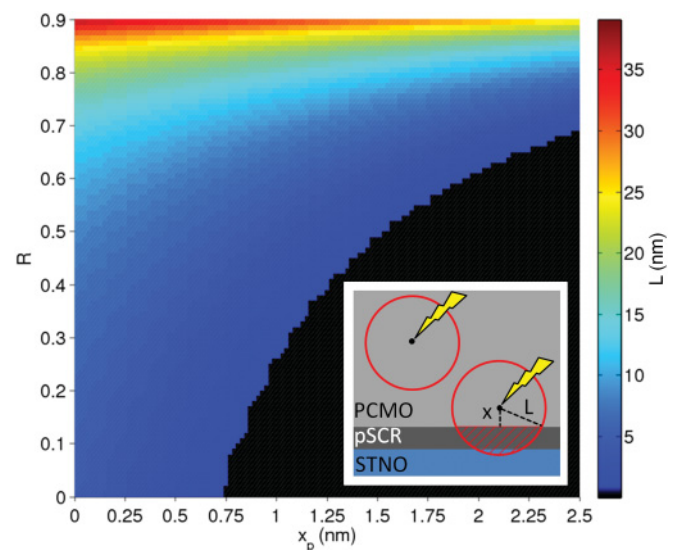


FIG. 7. (Color) Diffusion length  $L$  of photoexcited electrons in PCMO as a function of the junction recombination rate  $R$  and the p-SCR width  $x_p$ . Data are calculated from the comparison of the photocurrent and the spatiotemporal distribution of photogenerated carriers according to Eq. (5) for the 380-nm PCMO sample with  $y = 0.002$ . Inset: Basic constituents of the random-walk model of the diffusion process (see text).

dimensionless recombination rate  $R$ , which also subsumes potential recombination paths in the pSCR or at the very interface. All photoelectrons generated inside the pSCR are accelerated toward the interface in the built-in electric field and potentially contribute to the photocurrent. As stated above, the actual width of the pSCR is in the range  $x_p = 0.2\text{--}2.5$  nm. The contribution to  $I_{\text{SC}}^{\text{low}}$  of photocarriers from PCMO outside the pSCR is governed by diffusion, since no external field is applied. In the following, this diffusion process is modeled as a three-dimensional random walk, which appears to be a valid simplification since the local density gradients  $\partial g/\partial z$  turn out to be rather small ( $\Delta g/g < 10\%$  on a 10-nm scale). According to the inset in Fig. 7, the probability for a diffusing photocarrier to reach the pSCR as a function of its distance  $x$  reads  $w(x, L) = (1 - x/L)/2 - x^3/4L^3 \cdot (x^2/L^2 - 1)$  (interpenetrating volume divided by full sphere volume). Given the junction recombination rate  $R$  and the width  $x_p$  of the pSCR, the diffusion length  $L$  is varied to yield the measured low-energy photocurrent density:

$$n_{\text{SC}}^{\text{low}} = (1 - R) \cdot \int d\lambda \left\{ \int_{d-x_p}^d g(z, \lambda) dz + \int_{d-x_p-L}^{d-x_p} g(z, \lambda) \cdot w(d - x_p - z, L) dz \right\}. \quad (5)$$

Here,  $d$  denotes the PCMO film thickness and the integration over the photon wavelength runs through 540–2500 nm (2.3–0.5 eV).

Figure 7 displays the result of this analysis for the room-temperature data on the 380-nm PCMO absorber on  $y = 0.002$  STNO substrate spanning the full  $R\text{--}x_p$  range. At low  $R$  and a wide pSCR, the photocurrent exclusively stems from excitations within the pSCR [the first integral in Eq. (5)] as represented by the black area. In this case, the photoexcited electrons from the PCMO cannot diffuse to the pSCR within their lifetime. Reducing  $x_p$  and increasing  $R$  require additional inflow of photocarriers from the PCMO, and diffusion lengths of the order of 10 nm emerge. Similar numbers are found for the thinner, 200-nm PCMO sample demonstrating the consistency of the analysis. The determined diffusion length thus turns out to be an order of magnitude smaller than the PCMO film thicknesses used in this study. Therefore, the major part of the absorber merely acts here as a dimmer [compare the light penetration depth in Fig. 3(a)], and most of the excited carriers remain unused in terms of photovoltaic energy conversion. This is also reflected in the efficiency of the solar cells, which is between  $10^{-7}\%$  and 0.005%, depending on the absorber thickness and the temperature. It could be largely improved by optimization of the film thickness or the geometry of the shading contact or appropriate nanostructuring.

It is evident from Fig. 7 that proper knowledge of the junction recombination rate  $R$  is essential to decide whether significant contributions to the photocurrent stem from the PCMO film outside the pSCR. A strong hint of such contributions arises from the comparison of  $I_{\text{SC}}^{\text{low}}$  for CER-affected and -unaffected samples. As stated above,  $I_{\text{SC}}^{\text{low}}$  vanishes for the latter at low temperatures, which could be related to the decreasing mobility of the photo-carriers inside the PCMO

film upon charge ordering. However, the photocurrent remains constant also at low temperatures by virtue of the CER in the 200-nm thin sample, thus indicating the important contribution of mobile carriers from the PCMO film to the photocurrent. Such essentially temperature-independent characteristics of photoexcited carriers in the CER regime is a rather puzzling observation, which demands further investigations. At least, a pronounced lowering of the apparent activation energy for polaron hopping has been reported for the CER regime compared to the charge-ordered phase.<sup>7</sup>

Combining the diffusion length  $L = \sqrt{\tau D}$  and the Einstein relation for the diffusion coefficient  $D = \mu k_B T/e$  with the mobility  $\mu = 0.015$  cm<sup>2</sup>/Vs, typical for majority carriers in PCMO at room temperature ( $\mu = 1/\rho e p$  with resistivity  $\rho = 0.1$   $\Omega$  cm and effective carrier density  $p = 4 \times 10^{21}$  cm<sup>-3</sup>), photocarrier lifetimes  $\tau = 1\text{--}30$  ns correspond to the estimated  $L = 5\text{--}35$  nm. Wu *et al.* report on photocarrier lifetimes of 500 ns in the roomtemperature small-polaron regime of La<sub>0.6</sub>Ca<sub>0.4</sub>MnO<sub>3</sub> thin films,<sup>40</sup> which points to strongly reduced mobilities of excess carriers, e.g., by localization at acceptor defects.<sup>28</sup> In future work, direct experimental access to these important questions of nanoscale carrier diffusion and recombination could be provided by high-resolution electron-beam-induced current measurements as demonstrated by Han *et al.*<sup>41</sup>

#### IV. SUMMARY

Our combined study of the PCMO-STNO  $pn$  heterojunction reveals detailed information about its atomic and electronic structure and the related electrical transport properties. We found a difference in the materials' electron affinities of  $\Delta\chi = 0.65(4)/0.57(5)$  eV at temperatures of  $T = 300/80$  K constituting an interfacial energy spike in the conduction band. Despite the slight Mn/Ti interdiffusion, on a 2.5-nm scale, this energy spike dominates the electrical transport across the junction, which is e.g., reflected in the determined activation energies. A robust photovoltaic effect prevails at all temperatures in the interval  $T = 5\text{--}300$  K, most remarkably also in the band-gap-free  $Pnma$  phase of the PCMO. The emergence of the CER effect at low temperatures proves to have a pronounced impact on the photovoltaic properties, namely, a drop in the open-circuit voltage due to an appropriate decline in the activation energy and an enhancement of the photocurrent via preservation of carrier mobilities. We found evidence of important contributions to the photocurrent from photoexcitations within the PCMO bulk and estimated the corresponding photocarrier diffusion lengths to be on the scale of 1–10 nm.

#### ACKNOWLEDGMENTS

Funding of the Deutsche Forschungsgemeinschaft under Grant No. SFB602 is acknowledged by two of the authors (J.N. and C.J.). We thank S. Techert (MPI-BPC Goettingen) for support with optical spectroscopy. Work at BNL was supported by the US DOE, Office of Basic Energy Sciences, Materials Science and Engineering Division, under Contract No. DE-AC02-98CH10886.

- \*gesinesaucke@gmail.com; Now at Laboratory for Solid State Chemistry and Catalysis EMPA - Swiss Federal Laboratories for Materials Science and Technology, Ueberlandstrasse 129, CH-8600 Dübendorf, Switzerland.
- <sup>1</sup>W. Shockley and H. J. Queisser, *J. Appl. Phys.* **32**, 510 (1961).
  - <sup>2</sup>A. J. Nozik, *Physica E* **14**, 115 (2002).
  - <sup>3</sup>W. A. Tisdale, K. J. Williams, B. A. Timp, D. J. Norris, E. S. Aydil, and X.-Y. Zhu, *Science* **328**, 1543 (2010).
  - <sup>4</sup>O. Schirmer, M. Imlau, C. Merschjann, and S. B., *J. Phys. Condens. Matter* **21**, 123201 (2009).
  - <sup>5</sup>J. M. D. Coey, M. Viret, and v. S. Molnár, *Adv. Phys.* **48**, 167 (1999).
  - <sup>6</sup>W. Westhaeuser, S. Schramm, J. Hoffmann, and C. Jooss, *Eur. J. Phys. B* **53**, 323 (2006).
  - <sup>7</sup>S. Schramm, J. Hoffmann, and C. Jooss, *J. Phys. Condens. Matter* **20**, 395231 (2008).
  - <sup>8</sup>J. R. Sun, C. M. Xiong, T. Y. Zhao, S. Y. Zhang, Y. F. Chen, and B. G. Shen, *Appl. Phys. Lett.* **84**, 1528 (2004).
  - <sup>9</sup>B. T. Xie, Y. G. Zhao, C. M. Xiong, S. Park, and W. Wu, *Appl. Phys. Lett.* **92**, 232109 (2008).
  - <sup>10</sup>Z. G. Sheng, B. C. Zhao, W. H. Song, Y. P. Sun, J. R. Sun, and B. G. Shen, *Appl. Phys. Lett.* **87**, 242501 (2005).
  - <sup>11</sup>J. R. Sun, B. G. Shen, Z. G. Sheng, and Y. P. Sun, *Appl. Phys. Lett.* **85**, 3375 (2004).
  - <sup>12</sup>A. Sawa, T. Fujii, M. Kawasaki, and Y. Tokura, *Appl. Phys. Lett.* **86**, 112508 (2005).
  - <sup>13</sup>J. Dho, *Solid State Commun.* **150**, 2243 (2010).
  - <sup>14</sup>H. Inada, L. Wu, J. Wall, D. Su, and Y. Zhu, *J. Electron Microsc.* **58**, 111 (2009).
  - <sup>15</sup>M. Jaime, H. T. Hardner, M. B. Salamon, M. Rubinstein, P. Dorsey, and D. Emin, *Phys. Rev. Lett.* **78**, 951 (1997).
  - <sup>16</sup>S. H. Chun, M. B. Salamon, Y. Tomioka, and Y. Tokura, *Phys. Rev. B* **61**, R9225 (2000).
  - <sup>17</sup>R. Anderson, *Solid-State Electron.* **5**, 341 (1962).
  - <sup>18</sup>A. Linz, *Phys. Rev.* **91**, 753 (1953).
  - <sup>19</sup>T. Mitsui and W. B. Westphal, *Phys. Rev.* **124**, 1354 (1961).
  - <sup>20</sup>N. Biskup, A. de Andrés, J. L. Martinez, and C. Perca, *Phys. Rev. B* **72**, 024115 (2005).
  - <sup>21</sup>M. P. Kocher, D. A. Muller, and P. Rez, *Microsc. Microanal.* **9** (Suppl. 02), 842 (2003).
  - <sup>22</sup>M. Uijtewaal and P. Blöchl, personal communication (2011). The appropriate DFT calculations based on the PBE0<sup>r</sup> functional will be published elsewhere.
  - <sup>23</sup>D. W. Reagor, S. Y. Lee, Y. Li, and Q. X. Jia, *J. Appl. Phys.* **95**, 7971 (2004).
  - <sup>24</sup>L. F. Zagonel, M. Baeurer, A. Bailly, O. Renault, M. Hoffmann, J.-S. Shih, D. Cockayne, and N. Barrett, *J. Phys. Condens. Matter* **21**, 314013 (2009).
  - <sup>25</sup>L. Wu, R. F. Klie, Y. Zhu, and C. Jooss, *Phys. Rev. B* **76**, 174210 (2007).
  - <sup>26</sup>Y. Okimoto, Y. Tomioka, Y. Onose, Y. Otsuka, and Y. Tokura, *Phys. Rev. B* **57**, (R)9377 (1998).
  - <sup>27</sup>K. W. Blazey, *Phys. Rev. Lett.* **27**, 146 (1971).
  - <sup>28</sup>O. F. Schirmer, *J. Phys. Condens. Matter* **18**, R667 (2006).
  - <sup>29</sup>V. Ta Phuoc, R. Sopracase, G. Gruener, J. Soret, F. Gervais, A. Maignan, and C. Martin, *Mater. Sci. Eng. B* **104**, 131 (2003).
  - <sup>30</sup>A. Hamid, *Appl. Phys. A* **97**, 829 (2009).
  - <sup>31</sup>U. R. Singh, S. Chaudhuri, A. Dutta, R. C. Budhani, and A. K. Gupta, *Phys. Rev. B* **81**, 155120 (2010).
  - <sup>32</sup>K. Ebata, M. Hashimoto, K. Tanaka, A. Fujimori, Y. Tomioka, and Y. Tokura, *Phys. Rev. B* **76**, 174418 (2007).
  - <sup>33</sup>V. Nadenau, U. Rau, A. Jasenek, and H. W. Schock, *J. Appl. Phys.* **87**, 584 (2000).
  - <sup>34</sup>S. S. Perlman and D. L. Feucht, *Solid-State Electron.* **7**, 911 (1964).
  - <sup>35</sup>H.-W. Scheer and R. Schock, *Chalcogenide Photovoltaics: Physics, Technologies, and Thin Film Devices* (Wiley-VCH, New York, 2011), pp. 36–80, 72, 116.
  - <sup>36</sup>R. Scheer, *J. Appl. Phys.* **105**, 104505 (2009).
  - <sup>37</sup>A. Asamitsu, Y. Tomioka, H. Kuwahara, and Y. Tokura, *Nature* **388**, 50 (1997).
  - <sup>38</sup>S. Parashar, E. Ebenso, A. Raju, and C. Rao, *Solid State Commun.* **114**, 295 (2000).
  - <sup>39</sup>C. Jooss, L. Wu, T. Beetz, R. F. Klie, M. Beleggia, M. A. Schofield, S. Schramm, J. Hoffmann, and Y. Zhu, *Proc. Natl. Acad. Sci. USA* **104**, 13597 (2007).
  - <sup>40</sup>G.-R. Wu, M. Sasaki, T. Isa, H. Negishi, M. Inoue, W.-X. Gao, and G.-C. Xiong, *Solid State Commun.* **118**, 419 (2001).
  - <sup>41</sup>M.-G. Han, Y. Zhu, K. Sasaki, T. Kato, C. A. Fisher, and T. Hirayama, *Solid-State Electron.* **54**, 777 (2010).